

DSCA: A Dual-Stream Network with Cross-Attention on Whole-Slide Image Pyramids for Cancer Prognosis

Pei Liu, Bo Fu, Feng Ye, Rui Yang, Bin Xu, and Luping Ji

Abstract—The cancer prognosis on gigapixel Whole-Slide Images (WSIs) has always been a challenging task. To further enhance WSI visual representations, existing methods have explored image pyramids, instead of single-resolution images, in WSIs. In spite of this, they still face two major problems: high computational cost and the unnoticed semantical gap in multi-resolution feature fusion. To tackle these problems, this paper proposes to efficiently exploit WSI pyramids from a new perspective, the dual-stream network with cross-attention (DSCA). Our key idea is to utilize two sub-streams to process the WSI patches with two resolutions, where a square pooling is devised in a high-resolution stream to significantly reduce computational costs, and a cross-attention based method is proposed to properly handle the fusion of dual-stream features. We validate our DSCA on three publicly-available datasets with a total number of 3,101 WSIs from 1,911 patients. Our experiments and ablation studies verify that (i) the proposed DSCA could outperform existing state-of-the-art methods in cancer prognosis, by an average C-Index improvement of around 4.6%; (ii) our DSCA network is more efficient in computation—it has more learnable parameters (6.31M vs. 860.18K) but less computational costs (2.51G vs. 4.94G), compared to a typical existing multi-resolution network. (iii) the key components of DSCA, dual-stream and cross-attention, indeed contribute to our model's performance, gaining an average C-Index rise of around 2.0% while maintaining a relatively-small computational load. Our DSCA could serve as an alternative and effective tool for WSI-based cancer prognosis.

Index Terms—Computational Pathology, Cancer Prognosis, Survival Analysis, Multiple Instance Learning.

I. INTRODUCTION

Cancer prognosis typically answers the question of how the disease will develop for patients. It can be affected by various factors such as primary site, tumor grade, and treatment response [1]. Among these factors, some tumor-related ones can be uncovered by the histopathology Whole-Slide Image (WSI) from a high-end microscope [2], [3]. Thereby, WSIs are often utilized by doctors to assess patients' diseases and further make clinical decisions. Different from natural images,

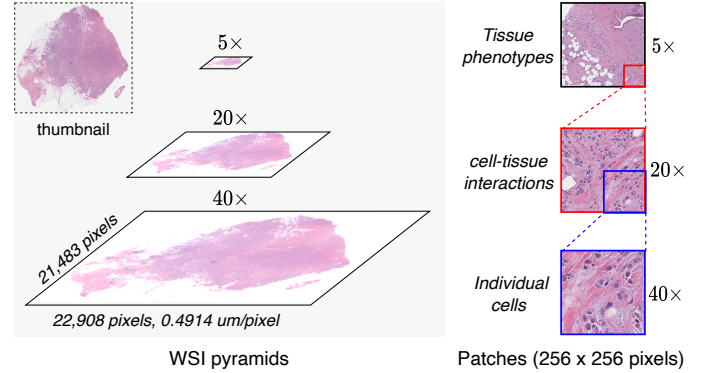


Fig. 1. Histopathology whole-slide image pyramids and their respective image patches.

medical WSIs are of extremely high-resolution, usually with gigapixel. And the WSIs at different magnifications present distinct microscopic views [2], [4]. These views can exhibit rich pathological entities, from tissue phenotypes (5 \times) to cellular organization (20 \times), and even to individual cells (40 \times), as shown in Figure 1.

Due to the gigapixel inherent in WSIs, a computational modeling paradigm is usually decomposed into: (i) slicing images into a myriad of small image patches and (ii) modeling these patches by using bag-level multiple instance learning (MIL) methods. In the early years, the most works of modeling WSIs for cancer prognosis focus on single-resolution images [5]–[11]. From a unified perspective, these works aim at making patch information flow within a specified structure to learn patch dependencies, and then outputting new patch embeddings to derive effective WSI representations, as shown in Figure 2(a). For example, Li *et al.* [6] originally adopt graph to describe patches. And they train a graph convolution network (GCN) to learn patch embeddings and WSI representations. Afterwards, more other patch structures (*e.g.*, cluster and sequence) and networks (*e.g.*, fully-connected networks and attention-based MIL networks) are further tried for WSI-based cancer prognosis [8], [9], [11], as illustrated in Figure 2(a). However, the single-resolution nature of these schemes greatly hinders models from fully utilizing inherent WSI pyramids (see Figure 1) for a more accurate cancer prognosis.

Motivated by pathologist's experience (examining WSIs from the region of interest to tumor localization) [2], as well as the idea of hierarchical vision representation [12], WSI-based

P. Liu, B. Fu, R. Yang, B. Xu, and L. Ji are with School of Computer Science and Engineering, University of Electronic Science and Technology of China, Xiyuan Ave, 611731 Chengdu, China. E-mail: yuukilp@163.com (Pei Liu).

F. Ye is with Institute of Clinical Pathology, West China Hospital, Sichuan University, Guo Xue Xiang, 610041 Chengdu, China.

* Corresponding author: Luping Ji (jiluping@uestc.edu.cn).

This manuscript is under review.

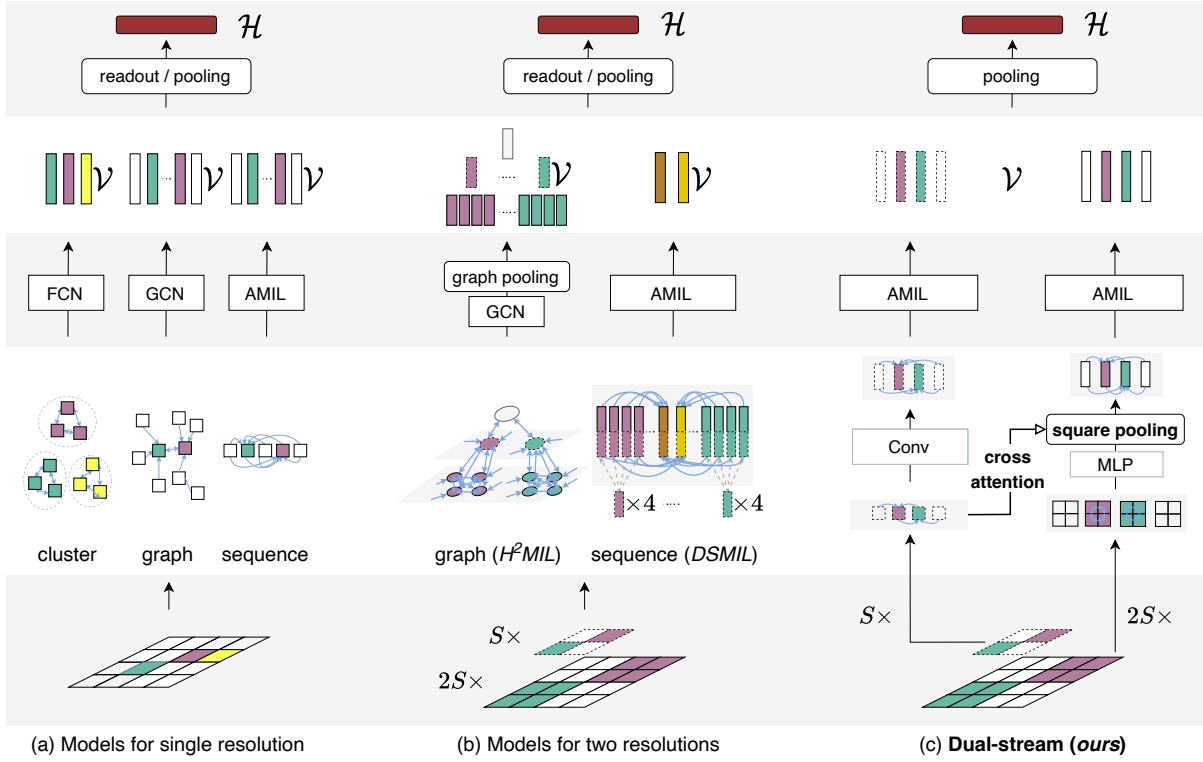


Fig. 2. Comparison of architectures. Colored patches are taken as examples to illustrate how networks process them. Blue line indicates patch aggregation flow. Dashed ones are low-resolution items. S denotes image resolution. \mathcal{V} is the set of patches after dependency learning. \mathcal{H} denotes WSI-level representation. AMIL means attention-based MIL network and MLP represents multi-layer perceptron. The details of (a) and (b) are available in Section II. The proposed architecture (c) is elaborated in Figure 3.

methods have gradually evolved into multi-resolution from single-resolution over recent years [4], [13]–[15]. DSMIL [14] is a representative multi-resolution scheme. It tries to utilize WSI pyramids by simply concatenating the patch features at different magnifications, as illustrated in Figure 2(b). By contrast, H^2MIL [15] adopts a multi-layer graph to describe multi-resolution patches. It specially builds cross-layer connections (or edges) for cross-resolution patches to integrate and exploit hierarchical features, as shown in Figure 2(b). Although these multi-resolution schemes have demonstrated better results than single-resolution ones, the way of *explicitly* using high-resolution patches throughout patch embedding learning is not efficient enough. Because there is usually an enormous amount of patches in high-resolution WSIs, whose number may be up to 10,000 at $20\times$ magnification. In addition, from the aspect of multi-scale feature fusion [16]–[18], existing schemes have not paid enough attention to the intrinsic semantical gap in different resolution patches, but are restricted to simple concatenating (DSMIL) or direct message passing (H^2MIL) for multi-resolution feature fusion.

To tackle the above issues, we propose an alternative scheme based on a totally different idea, dual-stream network with cross-attention (DSCA), as shown in Figure 2(c). This scheme is inspired by modern feature pyramid networks [16]–[19]. Briefly, our multi-resolution scheme consists of two vital components: dual-stream and cross-attention. The former is utilized to process low- and high-resolution patches respectively, so as to efficiently learn hierarchical WSI representation; the

latter handles the potential semantical gap in dual-resolution features. Specifically, in high-resolution stream, we devise a square pooling layer to largely decrease the number of high-resolution patches, exploiting fine-grained features efficiently. Furthermore, this square pooling is implemented by a cross-attention based method that pools high-resolution patches under the guidance of a global low-resolution one. Notably, our DSCA could be easily extended to multi-stream to model multi-resolution WSIs when its computational cost is feasible.

We summarize our main contributions as follows:

(1) A dual-stream network with cross-attention (DSCA) is proposed to learn hierarchical representations from WSI pyramids for cancer prognosis. Our DSCA has three highlights:

- We propose a novel scheme, a dual-stream network with cross-attention, to fully utilize image pyramids for enhancing the visual representation of WSIs. This scheme's key idea is quite distinct from other WSI-based multi-resolution ones.
- A square pooling layer is devised to significantly decrease the number of high-resolution patches, thus largely reducing the computational cost in network training.
- A cross-attention-based pooling method is proposed to pool high-resolution patches under the guidance of a global low-resolution one. It could effectively handle the potential semantical gap between high- and low-resolution features, making the fusion of dual-stream features smoother.

(2) A total of 3,101 WSIs from 1,911 patients, is used

TABLE I
WORKS RELATED TO WSI CLASSIFICATION OR CANCER PROGNOSIS.

Data Structure	Method	Task	Pyramid	Network	Highlights
cluster	WSISA (2017) [5]	prognosis		FCN	the first deep learning model
	DeepAttnMISL (2020) [8]	prognosis		FCN	end-to-end model; cluster attention
	BDOCOX (2021) [9]	prognosis		FCN	pseudo-bag; survival ranking loss
graph	DeepGraphSurv (2018) [6]	prognosis		SpectralGCN	the first graph-based model; adaptive graph
	RankSurv (2020) [7]	prognosis		HyperGCN	hyper-graph network; fixed graph
	PatchGCN (2021) [10]	prognosis		GCN	fixed regional graph
	H ² MIL (2022) [15]	classification	✓	GCN	attention GCN; iterative graph pooling
sequence	SeTranSurv (2021) [11]	prognosis		Transformer	self-supervised pretrained model; Transformer MIL
	DT-MIL (2021) [20]	classification		Transformer	deformable Transformer MIL
	TransMIL (2021) [21]	classification		Transformer	CNN positional encoding
	DSMIL (2021) [14]	classification	✓	Attention-MIL	the first patch pyramid model
	DTFD-MIL (2022) [22]	classification		Attention-MIL	pseudo-bag; CAM inspired patch aggregation
	HIPT (2022) [4]	both	✓	Transformer	hierarchical self-supervised pre-training
sequence	DSCA (ours)	prognosis	✓	Transformer	dual-stream; cross-attention; square pooling

to validate our scheme and compare it with state-of-the-art (SOTA) approaches. Our experimental results show that:

- The key idea, dual-stream and cross-attention, indeed contribute to DSCA's performance. It gains an average C-Index rise of around 2.0% while keeping relatively-small computational costs (1.61G–2.51G).
- Our DSCA network is more efficient than the H²MIL, a typical multi-resolution network. Namely, our network has more learnable parameters (6.31M vs. 860.18K) but less computational costs (2.51G vs. 4.94G).
- The proposed DSCA could outperform existing state-of-the-art methods in cancer prognosis, by an average C-Index improvement of around 4.6%.

II. RELATED WORK

This section will introduce (i) the image and feature pyramids in computer vision, (ii) traditional multiple instance learning (MIL) framework, and (iii) MIL-based WSI representation learning. To better compare the works related to WSI representation learning, we summarize some representative ones and exhibit them in Table I.

A. Image and Feature Pyramid

In computer vision, feature pyramids also refer to multi-scale or hierarchical features. It can be extracted from images to enhance visual representation. Traditional computer vision methods usually get feature pyramids from image pyramids by scaling original images [12]. By contrast, modern deep learning methods typically achieve this purpose by only using ConvNets [23], [24], not directly relying on image pyramids. Because ConvNets can produce feature maps with multi-scale receptive fields, showing a pyramidal shape. And these feature maps are inherent with hierarchical and semantically-distinct informations [25].

In order to effectively exploit the feature pyramids derived from the nature of deep neural networks, a typical solution [16]–[18] is to make multi-scale feature maps in the same scale via downsampling or upsampling operators, and then to add these feature maps for a multi-scale feature fusion.

However, as the approaches that use feature pyramids similarly, those existing multi-resolution schemes for learning WSI representation have not paid enough attention to better fuse multi-resolution patch features, but are restricted to a simple feature concatenating [14] or a direct message (feature) passing between graph nodes [15]. By contrast, our dual-stream scheme is inspired by the aforementioned way of deriving feature pyramids, and proposes to achieve the effective fusion of multi-resolution patches by using square pooling and cross-attention for gigapixel WSIs.

B. Multiple Instance Learning

Multiple Instance Learning (MIL) is a weakly-supervised learning framework [26], [27]. In MIL setting, the dataset, T , can be written by

$$T = \{(\mathcal{X}_i, y_i)\}_{i=1}^{i=N}, \quad \mathcal{X}_i = \{I_i^{(j)}\}_{j=1}^{j=n_i}, \quad (1)$$

where \mathcal{X}_i denotes a bag sample, y_i is the label of \mathcal{X}_i , and $I_i^{(j)}$ is the j -th instance of \mathcal{X}_i . A bag sample contains multiple instances and only bag labels are available. Traditional MIL approaches can be divided into bag-level MIL and instance-level MIL [28]. And the former aims to learn bag-level representation.

In WSI modeling, WSIs and patches can be viewed as bags and instances, respectively. Thus, most WSI-based approaches are also cast as MIL. Moreover, these approaches belong to bag-level MIL, focusing on learning WSI-level representation. We will review them in the following part.

C. WSI-level Representation Learning

1) *Single-resolution*: The schemes in this class usually use the WSIs at 20× magnification, since this resolution is enough to capture cell-tissue interactions and its computational cost is reasonable. To learn WSI-level representation, these schemes often learn patch dependencies at first and then aggregate all patch embeddings into WSI-level features, as shown in Figure 2(a). In patch dependency learning, patches are often organized as cluster, graph, or sequence (referring to those patches without any specified structures). (i) Cluster-based

schemes [5], [8], [9] often adopt patch similarity for clustering, and then learn patch dependencies in each cluster using fully-connected networks. (ii) Graph-based schemes [6], [7], [10] turn to adopt graph to construct patch dependencies. They pass or aggregate patch-level features along graph edges using GCNs. (iii) Sequence-based schemes [11], [20], [21] don't limit any structure for patches, *i.e.*, their models are structure-free. They learn all possible dependencies via attention-based networks, *e.g.*, Transformer [29], Attention-MIL [30], or Vision Transformer (ViT) [31]. WSI-level representation is usually obtained from patch-level embeddings by a global pooling operator at the end. However, the single-resolution nature of these various schemes could hinders models from fully utilizing WSI pyramids (see Figure 1).

2) **Multi-resolution**: Both DSMIL and H²MIL belong to this class, as shown in Figure 2(b). In sequence-based DSMIL, multi-resolution features are simply concatenated for patch dependency learning. And only those selected key patches could have connections with other patches. In graph-based H²MIL [15], the edges between low- and high-resolution patches are built additionally, compared to those graph-based single-resolution models. However, these cross-resolution edges can only transfer patch features directly, and the intrinsic semantic gap between different resolution patches still remains when calculating WSI-level features using global patch pooling. Most recently, the HIPT [4], built upon ViT, also utilizes WSI pyramids and has achieved promising results on WSI classification and prognosis. But this method focuses on studying a hierarchical *self-supervised pre-training strategy* for WSIs, which is distinct from the topic of this paper.

It is worth noting that, among the approaches exhibited in Table I, DSMIL and DTFD-MIL *can only be used for classification*, because DSMIL selects key patches using class scores and DTFD-MIL relies on class-specific CAMs [32]. In addition, as the most popular tasks on WSIs—classification and prognosis, there are much differences between them. For example, most classification-oriented models [33]–[36] focus on identifying a specific tumor stage or subtype. Although tumor stage and subtype are well-defined prognostic factors, prognosis models [37], [38] are typically required to gather more evidence for predicting survival accurately, such as the certain traits of cancer cells and the tumor surrounding micro-environmental cues in tissues [39], [40]. This means that actual prognostic patterns may be more complex in patient's WSIs. And these factors can vary across cancer types and individuals due to tumor heterogeneity and patient diversity [41], [42], thus leaving the cancer prognosis on WSIs as a more difficult task. We will discuss more through empirical experiments.

III. METHODOLOGY

Our DSCA architecture (see Figure 3) has four key components: token embedding layer, dependency learning layer, dual-stream fusion, and prediction layer, from input to output. The first two components are dual-stream version, as shown in Figure 3(b). The network architecture of two sub-streams roughly follows the philosophy of ViT [31].

A. Problem Formulation

1) **Dataset**: We denote our dataset by

$$T = \{(\mathcal{P}_i, t_i, c_i)\}_{i=1}^{i=N}, \mathcal{P}_i = \{p_i^{(j)}\}_{j=1}^{j=m_i}, \quad (2)$$

where \mathcal{P}_i , t_i , and c_i are the WSI material, follow-up time, and censorship status of i -th patient, respectively. $p_i^{(j)}$ denotes the j -th patch data in \mathcal{P}_i . And m_i is the number of patches in \mathcal{P}_i , which could be different across patients. Throughout the paper, the word patch means the *image patch* sliced from WSIs, whereas the word token means the *feature vector* corresponding to that patch.

2) **Dual-resolution**: The dual-resolution patches from WSI pyramids are used in our DSCA network. Without loss of generality, we denote the magnification of patches with lower resolution by $S\times$, and that with higher resolution by $\lambda S\times$, where the typical values of λ can be 2, 4, and 8. The subscript l and h indicate the item from *low-resolution* and *high-resolution*, respectively.

3) **WSI-level Cancer Prognosis**: Only with WSI-level labels, DSCA needs to learn WSI-level representation from multiple dual-resolution patches for cancer prognosis prediction in a weakly-supervised manner. As similar as bag-level MIL, WSI-level representation learning also has two essential steps: patch embedding learning and global patch pooling (or aggregation).

B. Spatially-aligned Dual-resolution Patching

First of all, we derive patches from the WSIs at two magnifications. The illustration of WSI pre-processing can be found in Figure 3(a). Specifically, for one WSI, we slice it at low resolution ($S\times$) and obtain the image patches with $a \times a$ pixels (a is 256 usually). Then we slice the same WSI at high resolution ($\lambda S\times$), generating patches with $a \times a$ pixels similarly. Moreover, as shown in Figure 3(a), a $S\times$ patch is exactly spatially-aligned to the λ^2 patches at $\lambda S\times$ (*i.e.*, a square of $\lambda \times \lambda$ cells). Following [43], we finally use a truncated ResNet-50 model [24] pre-trained on ImageNet [44] to extract instance features from each patch.

Given one patient with multiple WSIs, we denote its processed patch tokens at $S\times$ and $\lambda S\times$ by

$$\mathbf{X}_l \in \mathbb{R}^{m \times d} \text{ and } \mathbf{X}_h \in \mathbb{R}^{\lambda^2 m \times d},$$

respectively, where m is the number of $S\times$ patches and d is the dimensionality of token. Comparing with \mathbf{X}_h , \mathbf{X}_l contains coarser features and its receptive field is larger. Conversely, \mathbf{X}_h can provide more fine-grained and local information. This complementary nature thereby helps to enhance the visual representation of images.

C. Dual-stream Token Embedding

1) **Low-resolution Stream**: For this stream, we adopt a one-dimensional convolution layer as its token embedding layer for simplicity. \mathbf{X}_l is padded with zeros to keep the resolution at first. We write the output of this convolution layer by

$$\mathbf{E}_l = \text{Conv1D}(\mathbf{X}_l; k, s), \quad (3)$$

where $\mathbf{E}_l \in \mathbb{R}^{m \times d_e}$ and $d_e (< d)$ is the dimensionality of token embedding. k and s denote kernel size and stride

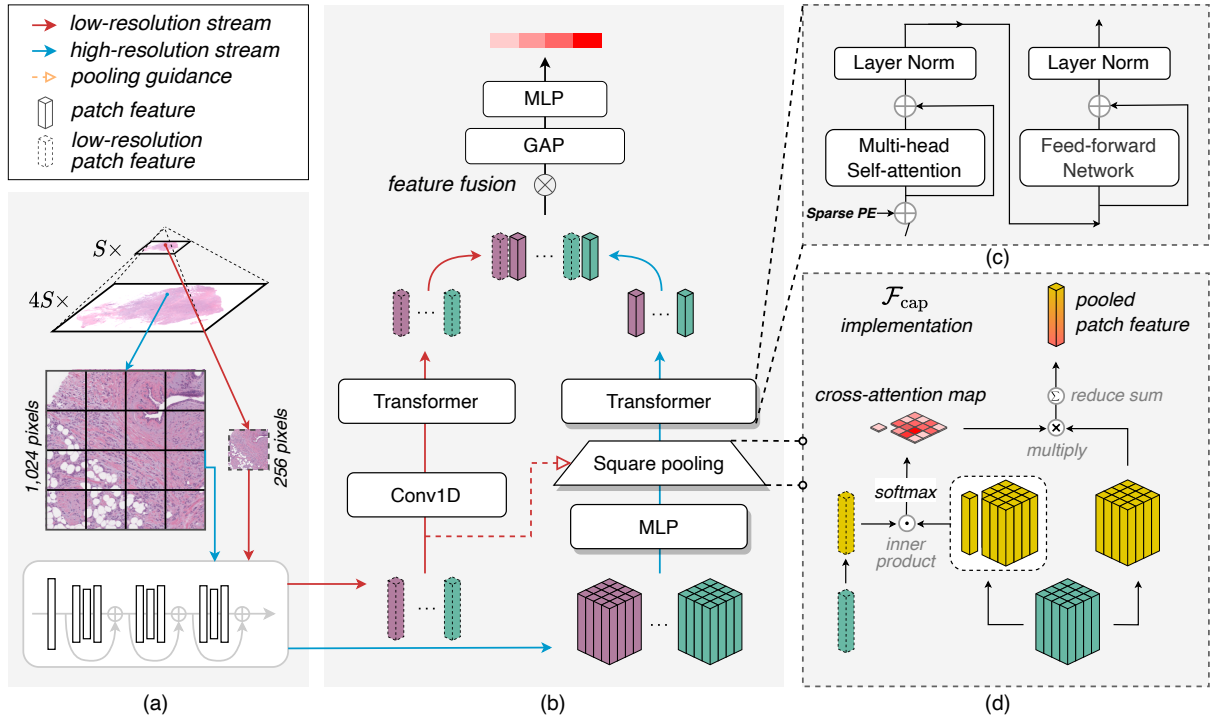


Fig. 3. Overview of our DSCA scheme (best viewed in color). We illustrate our scheme using $\lambda = 4$ and $\alpha = 256$. (a) Spatially-aligned dual-resolution patching: $S \times$ and $4S \times$ image are sliced into non-overlapping patches and their features are extracted by a pre-trained model. (b) DSCA architecture. (c) Transformer encoder in DSCA. (d) Cross-attention pooling \mathcal{F}_{cap} : it's an implementation of square pooling that pools high-resolution tokens under the guidance of low-resolution ones.

length, respectively. Conv1D can also play a role of dimension reduction in token embedding. Moreover, 1D-convolution can integrate individual patches within overlapping convolution windows, hence outputting overlapping token embeddings. This way could help to obtain more local continuity in tokens, as demonstrated in [19].

2) High-resolution Stream: In the high-resolution stream used for $\lambda S \times$ patches, we take all the tokens in a $\lambda \times \lambda$ square as a unit, and employ a token embedding operator for all units. Specifically, firstly we reshape \mathbf{X}_h into the sequence with square unit, which implements the function, $\text{resize} : \mathbb{R}^{\lambda^2 m \times d} \rightarrow \mathbb{R}^{m \times \lambda \times \lambda \times d}$. The reshaped input then goes through a token embedding layer and an activation layer in turn, written as

$$\begin{aligned} \mathbf{O}_h &= \sigma(\rho(\text{resize}(\mathbf{X}_h))), \\ \rho : \mathbb{R}^{m \times \lambda \times \lambda \times d} &\rightarrow \mathbb{R}^{m \times \lambda \times \lambda \times d_e}, \end{aligned} \quad (4)$$

where $\mathbf{O}_h \in \mathbb{R}^{m \times \lambda \times \lambda \times d_e}$ and σ is an activation function. We use a simple implementation, multi-layer perceptron (called MLP), for ρ . MLP calculates each token embedding individually, thereby generating compact token embeddings without keeping local continuity. It's worth noting that, here we don't adopt a convolution-based implementation to produce overlapping embedding, as similar as that in low-resolution stream. Because in high-resolution stream, overlapping embedding may have greater potential to incur more information redundancy, since gigapixel WSIs have obviously-lower information density than common images. We will further discuss this through experiments.

D. Square Pooling with Cross-attention

After high-resolution token embedding, we further apply a square pooling layer implemented by cross-attention to high-resolution tokens (\mathbf{O}_h), in view of the two reasons: (i) significantly decreasing the number of high-resolution tokens, thus enabling the closely-followed Transformer to learn token dependency efficiently; (ii) handling the potential semantical gap between low- and high-resolution tokens via a cross-attention mechanism, so as to make the fusion of two resolution tokens smoother.

Specifically, our token pooling operator is similarly applied to square units, defined by $\mathcal{F} : \mathbb{R}^{m \times \lambda \times \lambda \times d_e} \rightarrow \mathbb{R}^{m \times d_e}$. As illustrated in Figure 3(d), we implement a cross-attention-based method for \mathcal{F} , written as \mathcal{F}_{cap} . In short, \mathcal{F}_{cap} uses the attention scores mapped from dual-stream tokens to perform a weighted pooling for high-resolution tokens. Namely, our square pooling with cross-attention is implemented by

$$\begin{aligned} \mathbf{Q}_l &= \mathbf{X}_l \mathbf{W}_l, \\ \mathbf{E}_h &= \mathcal{F}_{\text{cap}}(\mathbf{O}_h; \mathbf{Q}_l), \end{aligned} \quad (5)$$

where $\mathbf{E}_h \in \mathbb{R}^{m \times d_e}$ and $\mathbf{W}_l \in \mathbb{R}^{d \times d_e}$. \mathbf{W}_l is a projection matrix to make the token dimension of \mathbf{Q}_l same to \mathbf{O}_h . Moreover, taking a low-resolution token (denoted as $\mathbf{z}_l \in \mathbb{R}^{1 \times d_e}$) and its respective high-resolution tokens (denoted as $\mathbf{z}_h \in \mathbb{R}^{\lambda^2 \times d_e}$) as examples, \mathcal{F}_{cap} can be written by

$$\mathcal{F}_{\text{cap}}(\mathbf{z}_h; \mathbf{z}_l) = \text{softmax} \left(\frac{\mathbf{z}_l \mathbf{W}_q (\mathbf{z}_h \mathbf{W}_k)^T}{\sqrt{d_e}} \right) \mathbf{z}_h \mathbf{W}_v, \quad (6)$$

where $\mathbf{W}_q, \mathbf{W}_k, \mathbf{W}_v \in \mathbb{R}^{d_e \times d_e}$ are the projection matrices for query, key, and value, respectively.

Our cross-attention scheme actually does a spatial attention pooling for big region ($\lambda a \times \lambda a$ pixels). It enables the high-resolution tokens with local and fine-grained features to pool under the guidance of a token with global view. Therefore, the result of cross-attention pooling is expected to selectively preserve certain fine-grained information based on the spatial response of high-resolution patches to their global view. In addition, with the square pooling, the number of high-resolution tokens can be decreased by a factor of $\frac{1}{\lambda^2}$, becoming identical to the number of low-resolution ones.

E. Transformer-based Token Dependency Learning

1) *Sparse Positional Embedding*: We calculate the positional embedding (PE) of tokens as similar as [29], rather than ViT. Because the size of tokens (*i.e.*, the value of m) varies across WSIs, which is different from general cases. In addition, we filter the patches without any tissue region in WSI patching, thus bringing the problem of spatially-sparse distribution in tokens.

To solve this, we put all WSIs from one patient in a row and then map the coordinates of all available patches to a discrete domain without breaking their relative locations. In this way, we can encode the position information of tokens while preserving intrinsic spatially-sparse property, even for multiple WSIs. For simplicity, we write the result of sparse PE as

$$\mathbf{PE} \in \mathbb{R}^{m \times d_e}.$$

2) *Dependency Learning*: As shown in Figure 3(c), we employ a Transformer encoder at the end of either stream to learn potential token dependencies, as Transformer has achieved great success in capturing token dependencies [29]. This encoder is a vanilla Transformer encoder that consists of a multi-head self-attention layer and a feed-forward network. We denote these two parts by $\text{MSA} : \mathbb{R}^{m \times d_e} \rightarrow \mathbb{R}^{m \times d_e}$ and $\text{FFN} : \mathbb{R}^{m \times d_e} \rightarrow \mathbb{R}^{m \times d_e}$, respectively. The Transformer encoder, $\mathcal{T} : \mathbb{R}^{m \times d_e} \rightarrow \mathbb{R}^{m \times d_e}$, can be expressed by

$$\begin{aligned} \mathcal{T} &= \zeta \circ \varphi, \\ \zeta(x) &= \text{LN}(\text{MSA}(x) + x), \\ \varphi(x) &= \text{LN}(\text{FFN}(x) + x), \end{aligned} \quad (7)$$

where LN is a layer normalization function [45]. Based on Equation 7, we can get the outputs as follows:

$$\mathbf{V}_l = \mathcal{T}_l(\mathbf{E}_l + \mathbf{PE}) \text{ and } \mathbf{V}_h = \mathcal{T}_h(\mathbf{E}_h + \mathbf{PE}).$$

F. Dual-stream Feature Fusion

Stream feature fusion (FF) is implemented by the following function:

$$\mathbf{F} = \text{FF}(\{\mathbf{V}_l, \mathbf{V}_h\}). \quad (8)$$

We use a simple implementation of FF, concatenating dual-resolution tokens, defined by

$$\text{cat} : \mathbb{R}^{2m \times d_e} \rightarrow \mathbb{R}^{m \times 2d_e}.$$

We also consider an adding version of FF. Its result is shown in experiments.

G. Prognosis Prediction

1) *Output Layer*: We utilize a global attention pooling (GAP) [30] to obtain WSI-level features. Specifically, all available tokens are weighted by calculating attention scores, and then they are aggregated into a global vector. This global vector is finally employed to infer prognosis prediction via a multi-layer perceptron (MLP). Our output layer implements

$$\begin{aligned} \mathbf{H} &= \text{GAP}(\mathbf{F}), \\ \mathbf{O} &= \text{sigmoid}(\text{MLP}(\mathbf{H})), \end{aligned} \quad (9)$$

where $\text{GAP} : \mathbb{R}^{m \times d_o} \rightarrow \mathbb{R}^{d_o}$, $\text{MLP} : \mathbb{R}^{d_o} \rightarrow \mathbb{R}^{n_t}$, and $\mathbf{O} \in \mathbb{R}^{n_t}$ is the prediction of individual hazard function. d_o is the dimensionality of WSI-level features, which equals to $2d_e$. n_t denotes the number of time points in prediction.

2) *Loss Function*: The loss function for optimizing our DSCA network is a negative log-likelihood function [46] used for training discrete deep survival models:

$$\begin{aligned} L &= L_{\text{uncensored}} + (1 - \alpha)L_{\text{censored}}, \\ L_{\text{uncensored}} &= - \sum_{(\mathcal{P}_i, t_i, c_i) \in T} \left\{ (1 - c_i) \cdot \log(S(t_i - 1) \cdot h(t_i)) \right\}, \\ L_{\text{censored}} &= - \sum_{(\mathcal{P}_i, t_i, c_i) \in T} \left\{ c_i \cdot \log(S(t_i)) \right\}, \end{aligned} \quad (10)$$

where $\alpha \in \mathbb{R}_0^+$, $h(t_i)$ is the t_i -th element of the network prediction \mathbf{O} , and $S(t_i) = \prod_{s=1}^{t_i} (1 - h(s))$. In survival analysis, $h(t)$ is a hazard function, and $S(t)$ is a survival function indicating the probability of surviving time t . This survival function doesn't rely on any assumption about the form of hazard function. By contrast, the popular loss functions [47], [48], based on Cox model, have a strong assumption—proportional hazard. We thereby adopt Equation 10 to optimize DSCA, as suggested in [46].

IV. EXPERIMENTS

A. Datasets

We validate DSCA on the three publicly-available datasets: National Lung Screening Trial (NLST) [49], BRCA Cancer (BRCA), and Low-Grade Glioma (LGG). The last two datasets are from The Cancer Genome Atlas [50]. As shown in Table II, we obtain a total of 3,101 WSIs from 1,911 patients, after excluding the patients with unknown follow-up status or unavailable WSIs. Note that there isn't any other form of data curation except that we mentioned.

TABLE II
STATISTIC OF DATASETS.

Name	NLST	TCGA	
		BRCA	LGG
overall	primary site	lung	breast
	storage size	0.76 TB	0.98 TB
	death ratio	35.9%	13.5%
	# patients	447	978
5×	# WSIs	1,222	1,043
	# patches	247,209	201,780
	# patches / # WSIs	202.3	193.5
			164,841
20×	# patches	3,955,344	3,228,480
	# patches / # WSIs	3,236.8	3,095.4
			2,637,456
			3,154.9

TABLE III
PROGNOSIS PREDICTION PERFORMANCE MEASURED BY 5-FOLD CROSS-VALIDATION.

Method	Mean C-Index (Standard Deviation)			Model Size	# MACs
	NLST	BRCA	LGG		
Deep Sets (2017) [51]	0.47271 (0.08325)	0.47106 (0.03884)	0.60080 (0.07250)	657.16K	1.76G
Attention-MIL (2018) [30]	0.57157 (0.09022)	0.54118 (0.06273)	0.60820 (0.04624)	920.07K	2.64G
DeepAttnMISL (2020) [8]	0.55062 (0.06372)	0.53234 (0.03403)	0.61963 (0.05941)	1.18M	1.77G
DeepGraphConv (2018) [6]	0.57931 (0.06061)	0.54254 (0.07946)	0.61954 (0.07918)	790.02K	2.42G
Patch-GCN (2021) [10]	0.58588 (0.08245)	0.49325 (0.02457)	0.67261 (0.01605)	1.38M	3.75G
SeTranSurv (2021) [11]	0.54203 (0.10244)	0.55339 (0.09756)	0.59912 (0.03948)	1.58M	1.22G
TransMIL* (2021) [21]	0.59535 (0.03053)	0.53175 (0.06944)	0.69049 (0.05121)	2.67M	9.55G
H ² MIL* (2022) [15]	0.60129 (0.03948)	0.53125 (0.05582)	0.56867 (0.11425)	860.18K	4.94G
DSCA (ours)	0.66803 (0.05817)	0.61224 (0.05350)	0.70181 (0.04321)	6.31M	2.51G

* Originally proposed for WSI classification. Baseline comparisons are elaborated in Section IV-B.5. The # MACs of model are measured using a bag with 210 patches at low resolution and 3,360 patches at high resolution. We use the same patch feature extractor and loss function in all methods for fair comparisons.

From Table II, we can see that the overall death ratio of breast cancer is significantly smaller than that of the other two cancer diseases, statistically. The prognosis event of interest that we predict is the overall survival (OS), a typical endpoint in survival analysis. We can notice that there are usually more than 3,000 patches per WSI on average at 20 \times .

B. Experiment Setup

1) *Evaluation Metrics*: We adopt Concordance Index (C-Index) [52] to measure model performance. C-Index is a commonly-used evaluation metrics in survival analysis, which mainly evaluates the model ability in survival risk discrimination. It's written as

$$\text{C-Index} = \frac{1}{M} \sum_{i:c_i=0} \sum_{j:t_i < t_j} \mathcal{I}(\hat{y}_i > \hat{y}_j) \in [0, 1],$$

where $\mathcal{I}(\cdot)$ is an indicator function and M is the number of all comparable pairs. We compute \hat{y} by a negative average over the survival probabilities at all time points, *i.e.*, $\hat{y} = \frac{1}{n_t} \sum_{k=1}^{n_t} S(k)$. The C-Index would be larger if a model could predict higher risks for the patients who die earlier.

2) *Model Evaluation*: We use 5-fold cross-validation to evaluate all the models presented in our experiments. In each fold training, we retain the 20% training set as a validation set. All data splittings are ensured to conduct at patient-level. To assess model's computational efficiency, we report the size of trainable parameters (Model Size) and the theoretical amount of Multiply-Accumulate operations (# MACs) in models, using the package *ptflops* available in <https://pypi.org/project/ptflops>.

3) *Dual-resolution Setup*: We adopt 20 \times for high resolution in our experiments, because this resolution is a commonly-used choice in previous models, *e.g.*, [4], [6], [7], [9]–[11], [14], [20]–[22]. Moreover, this resolution could capture cell-tissue interactions for downstream prediction, and its computational cost is reasonable. In addition, we select 5 \times for low resolution, *i.e.*, $\lambda = 4$. Because this resolution can present tissue phenotypes [4] (see Figure 1), contributing to prognosis prediction.

4) *Implementation Details*: For WSI patching, we set the size of patch to 256 \times 256 pixels, *i.e.*, $a = 256$, following

previous works. And $d = 1024$, output by a truncated ResNet-50 model. In Conv1D, we empirically set $k = 5$ and $s = 3$. For each dataset we use the same settings: 150 epochs, a learning rate of 8×10^{-5} , a gradient accumulation step of 16, an optimizer of Adam with a weight decay rate of 5×10^{-4} , and a loss function given by Equation 10. Learning rate decays by a factor of 0.5 if validation loss doesn't decrease in past 10 epochs. Model training stops with patience of 30 epochs. For model architecture, we empirically set d_e as 384 and n_t as 4. All experiments run on a machine with 2 \times V100s GPUs.

5) *Baseline Comparisons*: Deep Sets [51] and Attention-MIL [30] are adopted as baselines since they are classical MIL approaches. And the approaches presented in Table I are also used for comparisons, *except*: (i) BDOCOX [9] and RankSurv [7]: source codes are unavailable; (ii) DSMIL [20] and DTFD-MIL [22]: inapplicable to prognosis tasks (see Section II-C). Moreover, WSISA [5] and DT-MIL [20] are not among our baselines, because the former is not a MIL model and the latter cannot be used for spatially-sparse patches. HIPT [4] is based on a pre-training strategy so it's also not used. Despite unavailable source codes, SeTranSurv [11] is also in our baselines, since it's the first Transformer-based prognosis model. And we use an inhouse-implementation for it.

C. Prognosis Prediction

1) *Overall Performance*: The results of model performance are shown in Table III. From this table, we can summarize that: (i) Our DSCA scheme achieves the best performances in C-Index on three datasets, and it shows obvious advantages on NLST and BRCA. (ii) Our DSCA model generally has more learnable parameters but fewer computational costs.

Furthermore, from Table III we have the following empirical analysis. (i) We can notice that the classification-oriented model, TransMIL, is very competitive with existing models. Because TransMIL specially devises a convolution-based positional encoding module to extract discriminative global features, as described in [21]. But this module also brings huge computational costs (9.55G MACs, see Table III). By contrast, our DSCA has an obviously-lower computational cost (2.51G MACs), owing to the square pooling layer which significantly decreases the number of high-resolution patches while fully

TABLE IV

ABLATION STUDY ON DSCA. RESULTS ARE OBTAINED BY 5-FOLD CROSS-VALIDATION. RES. REFERS TO RESOLUTION.

Dual-stream		Cross-attention	Mean C-Index			Model Size	# MACs
Low Res.	High Res.		NLST	BRCA	LGG		
✓	-	-	0.66174	0.60193	0.57553	3.15M	695.39M
-	✓	-	0.65914 - 0.00260	0.60820 + 0.00627	0.65614 + 0.08061	1.58M	1.61G
✓	✓	-	0.66887 + 0.00973	0.59599 - 0.01221	0.68965 + 0.03351	5.32M	2.43G
✓	✓	✓	0.66803 - 0.00084	0.61224 + 0.01625	0.70181 + 0.01216	6.31M	2.51G

utilizing fine-grained features. Moreover, our scheme also achieves better performance than TransMIL, especially on NLST and BRCA. (ii) As a multi-resolution scheme similar to our DSCA, the classification-oriented H²MIL performs not well in cancer prognosis. A possible reason is that H²MIL has too few learnable model parameters (860.18K) to handle the more complex task, cancer prognosis. Besides that, we can notice that, although H²MIL has few model parameters, its dense cross-resolution edges in graph (see Figure 2(b)) incur a high computation load (4.94G). Compared to explicitly using cross-resolution connections like H²MIL, our DSCA adopts cross-attention to deal with the potential semantical gap between dual-resolution patches. We will dive into our DSCA through ablation studies. (iii) Our DSCA gains a C-Index improvement of 6.7%, 5.9%, and 1.1% on NLST, BRCA, and LGG, respectively, in comparison with SOTA baselines. This empirical result demonstrates that the proposed DSCA could often outperform existing mainstream approaches in WSI cancer prognosis. We hope that our scheme could provide a strong baseline for WSI-based prognosis tasks.

2) *Risk Stratification*: We also assess the model’s ability in risk stratification, which is also a widely-used evaluation for survival analysis models. In the setting of risk stratification, patients are stratified into a high-risk group if their risk predictions are higher than the median; otherwise, patients are in a low-risk one.

into a high- or low-risk group with significant differences (P-Value<0.01). It means that our models could accurately identify a bad or good prognosis from the WSIs of cancer patients. Moreover, the stratification differences given by our method are more obvious than that given by others on NLST and BRCA, seen from P-Values.

D. Ablation Study

1) *Dual-stream and Cross-attention*: To study how the key components, dual-stream and cross-attention, affect DSCA’s performance, we start from a single-stream version that only processes single-resolution patches (*i.e.*, in which one sub-stream is removed from DSCA). Note that, for the DSCA only with high-resolution stream, we use a simple function, mean-pooling, to implement its square pooling layer. Then, we improve single-stream networks by completing dual-stream and further replacing mean-pooling with the proposed cross-attention pooling. Our results are shown in Table IV.

From Table IV, we can observe the following empirical facts. (i) Comparing high-resolution stream with low-resolution one, the C-Index on LGG has a clear rise (~ 0.08), and that on NLST and BRCA has no obvious changes (the highest is ~ 0.006). (ii) Transforming high-resolution stream into dual-stream, the C-Index on both LGG and NLST have improvement, and the improvement on LGG is more apparent (~ 0.03); whereas the C-Index on BRCA drops by ~ 0.01 (this drop is broken back by adding cross-attention). (iii) After further applying cross-attention pooling, the values of C-Index can be further increased, except the quite slight drop (< 0.001) on NLST. (iv) Moreover, from Table IV, we can also see that the model size of DSCA is greatly increased (from 1.58M to 6.31M) compared to the beginning version. This is due to the involvement of Conv1D. However, we also notice that the amount of MACs remains relatively-small (1.61G–2.51G), owing to our square pooling layer especially for enormous high-resolution patches. Finally, by combining these two vital components, our DSCA could often achieve the best performances on three datasets. This ablation study suggests that our key idea, dual-stream with cross-attention, indeed contributes to DSCA.

2) *High-resolution Token Embedding*: We compare the two different implementations of high-resolution token embedding layer (ρ), MLP and Conv2D, as discussed in Section III-C.2. Comparison results are shown in Table V. From these results, we can summarize that the high-resolution token embedding implemented by Conv2D generally doesn’t bring apparent positive effects on model performance (it only has

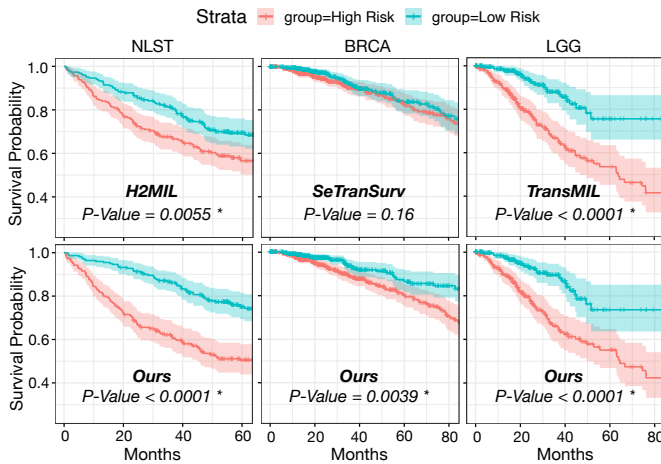


Fig. 4. Risk stratification. Our method and the other best ones (in C-Index) are shown. The survival curves are plotted using ground-truth labels. P-Value is computed by log-rank test to measure the significance of survival differences between two risk groups.

From Figure 4, we can see that our models, trained on three cancer types separately, can always classify patients

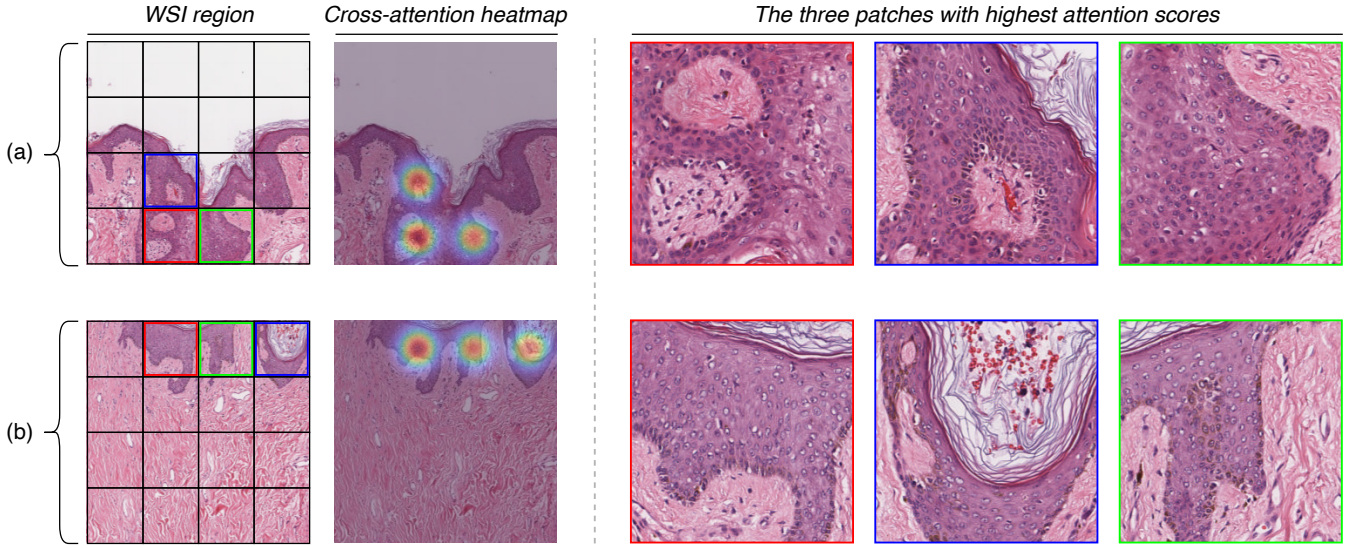


Fig. 5. Visualization of cross-attention maps on region (a) and (b). Patches are exhibited in descending order according to their attention scores. Each region patch is at $5\times$ magnification and with 256×256 pixels. The top attention patches are at $20\times$ magnification and with the same size.

an ignorable improvement of <0.002 on NLST); instead, it largely increases the model size by 3.14M and the # MACs by 10.57G, in comparison with MLP.

TABLE V
COMPARISON OF DIFFERENT TOKEN EMBEDDING LAYERS.

ρ	Mean C-Index			Model Size	# MACs
	NLST	BRCA	LGG		
MLP	0.66803	0.61224	0.70181	6.31M	2.51G
Conv2D	0.66981	0.58552	0.67344	9.45M	13.08G

These facts indicate that the way of overlapping embedding in Conv2D may not be suitable for high-resolution WSI patches though it has been demonstrated to be effective for common images [19]. By contrast, the compact token embedding in MLP is almost always shown to be better in both model performance and computation efficiency, which exactly demonstrates our argument (see Section III-C.2).

3) *Network Hyper-parameters*: We test the effect of some important network hyper-parameters on model performance, and show it as follows.

(1) *Sparse positional embedding (PE)*. The details of sparse PE can be found at Section III-E.1. We test the DSCA network with or without sparse PE, and show their results in Table VI. From this table, we can find that the network with sparse PE achieves the best performance on both NLST and BRCA; and on LGG, the network without sparse PE is better. We thereby use this PE setting in all experiments: applying sparse PE if it's on NLST or BRCA; and not if it's on LGG.

(2) *Stream feature fusion (FF)*. We also test different implementations for the feature fusion of dual-stream tokens (V_l and V_h): concatenating and adding. From the results shown in Table VII, we see that, only on NLST the way of adding leads over concatenating by a quite narrow margin (~ 0.004). Thus we uniformly set the stream FF of DSCA to concatenating on three datasets in all experiments.

TABLE VI
EFFECT OF SPARSE POSITIONAL EMBEDDING (PE).

Sparse PE	Mean C-Index		
	NLST	BRCA	LGG
✓	0.66803	0.61224	0.68740
✗	0.65901 - 0.00902	0.59148 - 0.02076	0.70181 + 0.01441

TABLE VII
EFFECT OF DIFFERENT FEATURE FUSION (FF) METHODS.

Stream FF	Mean C-Index		
	NLST	BRCA	LGG
concatenating	0.66803	0.61224	0.70181
adding	0.67216 + 0.00413	0.61115 - 0.00109	0.68121 - 0.02060

E. Interpretability and Visualization

To intuitively understand the effect of the cross-attention pooling used in DSCA, we randomly select two regions from breast cancer tissues, and visualize their cross-attention results. Specifically, at first we obtain cross-attention scores (averaged over multiple attention heads) from each $5\times$ region and its respective $20\times$ patches (presented as 4×4 cells), by using Equation 6. And then, we select the three patches with highest attention scores, and provide their cellular details. As shown in Figure 5, we can observe that, the cross-attention guided by global views could enable the model to focus on informative patches, *e.g.*, the patches with normal or tumorous cells. Moreover, almost all the top attention patches contain high-density irregular cells (they are highly-different in size and shape, see Figure 5), increasing the probability of cancer and poor prognosis [42]. Consequently, the model could distill fine-grained and most discriminative features from high-resolution patches via cross-attention pooling, thus realizing a more accurate prognosis prediction.

In addition, we further show the result of global attention

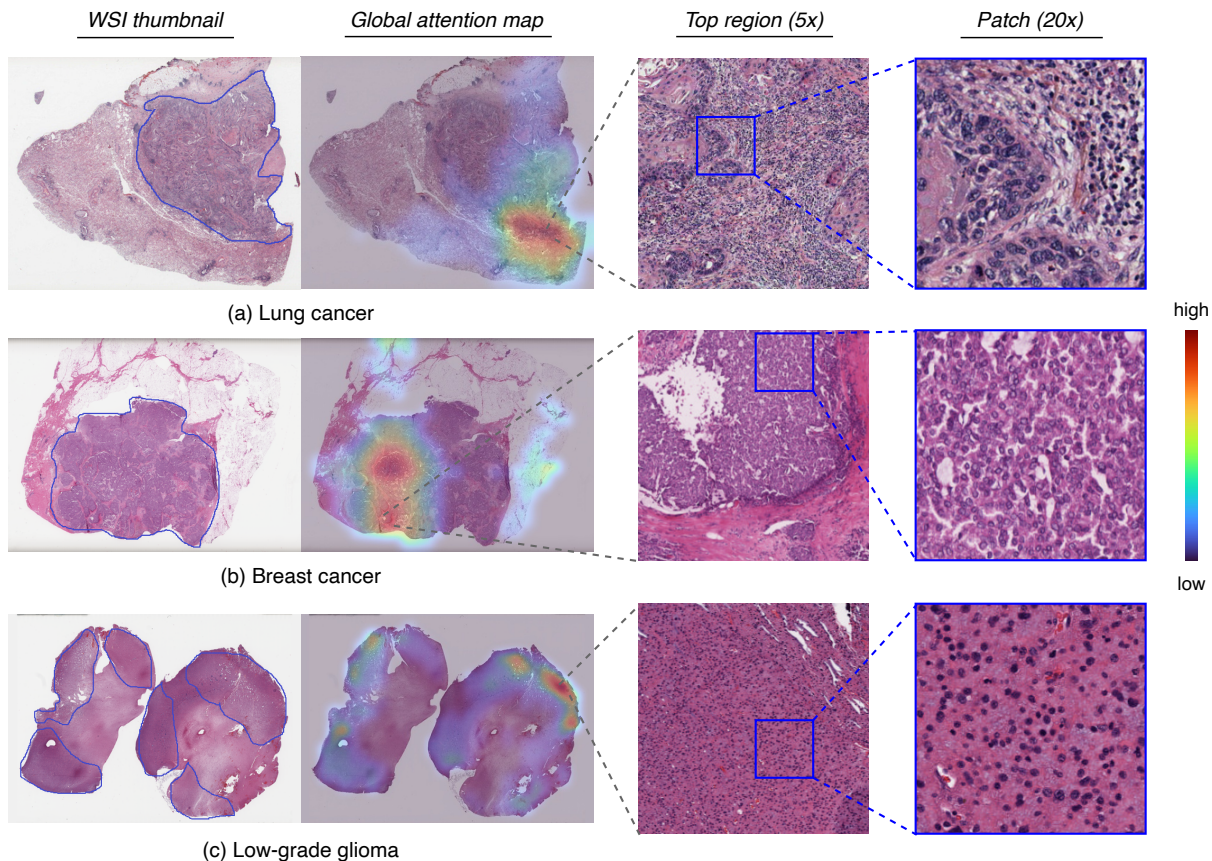


Fig. 6. Visualization of global attention maps on the three WSIs with different cancer diseases. The blue lines in WSI thumbnails are the annotations of the tumorous region of interest. The 50% of regions with lowest attention scores are reassigned with zero scores for a better view in global attention maps. A top region means a region with a top attention score.

pooling (see DSCA’s output layer), to observe which region could have high importance on cancer prognosis. As shown in Figure 6, our model could differentiate local regions for prognosis prediction, and those predicted hot regions tend to appear in RoI (region of interest) annotations. Taking a close look at hot regions and its enlarged patch images, we can see some highly-differentiated and irregular cells in them. Especially for the case of lung cancer, there are clear differences in cellular morphology between the cells located in the left side and the right side (see the 20 \times patch in Figure 6(a)). These observations suggest that our model could have a good interpretability for cancer prognosis.

V. CONCLUSION

This paper proposed a dual-stream network with cross-attention (DSCA) to fully utilize WSI pyramids for cancer prognosis. Unlike existing multi-resolution schemes for WSIs, we devised two sub-streams to process the patches with two resolutions. Moreover, we proposed a square pooling layer implemented by cross-attention to efficiently learn high-resolution features and make the fusion of dual-stream features smoother. The experimental results on three publicly-available datasets showed that our efficient DSCA could often outperform existing SOTA methods. And our key idea, dual-stream and cross-attention, indeed plays a vital role in predicting cancer patients’ overall survival. We hope that the

proposed DSCA could encourage more works to explore WSI pyramids for broad downstream tasks, and that our dual-stream architecture could serve as an effective option for WSI-based cancer prognosis.

In the future, we will explore other efficient strategies of multi-scale feature fusion for gigapixel WSIs, such as a reverse or bidirectional fusion of multi-resolution features. And we will also study how to utilize feature pyramids directly and efficiently in WSIs, similar to the way of modern ConvNets in common images. In view of the advancements in classical computer vision and WSI modeling, we believe that WSI pyramids would become a promising research topic in computational pathology.

REFERENCES

- [1] A. G. De Boer, T. Taskila, A. Ojajärvi, F. J. Van Dijk, and J. H. Verbeek, “Cancer survivors and unemployment: a meta-analysis and meta-regression,” *JAMA*, vol. 301, no. 7, pp. 753–762, 2009.
- [2] M. D. Zarella, D. Bowman, F. Aeffner, N. Farahani, A. Xthona, S. F. Absar, A. Parwani, M. Bui, and D. J. Hartman, “A Practical Guide to Whole Slide Imaging: A White Paper From the Digital Pathology Association,” *Archives of Pathology & Laboratory Medicine*, vol. 143, no. 2, pp. 222–234, 10 2018.
- [3] P. Bankhead, M. B. Loughrey, J. A. Fernández, Y. Dombrowski, D. G. McArt, P. D. Dunne, S. McQuaid, R. T. Gray, L. J. Murray, H. G. Coleman *et al.*, “Qupath: Open source software for digital pathology image analysis,” *Scientific reports*, vol. 7, no. 1, pp. 1–7, 2017.

- [4] R. J. Chen, C. Chen, Y. Li, T. Y. Chen, A. D. Trister, R. G. Krishnan, and F. Mahmood, "Scaling vision transformers to gigapixel images via hierarchical self-supervised learning," in *Proceedings of the IEEE/CVF Conference on Computer Vision and Pattern Recognition*, June 2022, pp. 16 144–16 155.
- [5] X. Zhu, J. Yao, F. Zhu, and J. Huang, "Wsisa: Making survival prediction from whole slide histopathological images," in *Proceedings of the IEEE Conference on Computer Vision and Pattern Recognition*, 2017, pp. 7234–7242.
- [6] R. Li, J. Yao, X. Zhu, Y. Li, and J. Huang, "Graph cnn for survival analysis on whole slide pathological images," in *International Conference on Medical Image Computing and Computer-Assisted Intervention*. Springer, 2018, pp. 174–182.
- [7] D. Di, S. Li, J. Zhang, and Y. Gao, "Ranking-based survival prediction on histopathological whole-slide images," in *International Conference on Medical Image Computing and Computer-Assisted Intervention*. Springer, 2020, pp. 428–438.
- [8] J. Yao, X. Zhu, J. Jonnagaddala, N. Hawkins, and J. Huang, "Whole slide images based cancer survival prediction using attention guided deep multiple instance learning networks," *Medical Image Analysis*, vol. 65, p. 101789, 2020.
- [9] W. Shao, T. Wang, Z. Huang, Z. Han, J. Zhang, and K. Huang, "Weakly supervised deep ordinal cox model for survival prediction from whole-slide pathological images," *IEEE Transactions on Medical Imaging*, vol. 40, no. 12, pp. 3739–3747, 2021.
- [10] R. J. Chen, M. Y. Lu, M. Shaban, C. Chen, T. Y. Chen, D. F. Williamson, and F. Mahmood, "Whole slide images are 2d point clouds: Context-aware survival prediction using patch-based graph convolutional networks," in *International Conference on Medical Image Computing and Computer-Assisted Intervention*. Springer, 2021, pp. 339–349.
- [11] Z. Huang, H. Chai, R. Wang, H. Wang, Y. Yang, and H. Wu, "Integration of patch features through self-supervised learning and transformer for survival analysis on whole slide images," in *International Conference on Medical Image Computing and Computer-Assisted Intervention*. Springer, 2021, pp. 561–570.
- [12] E. H. Adelson, C. H. Anderson, J. R. Bergen, P. J. Burt, and J. M. Ogden, "Pyramid methods in image processing," *RCA engineer*, vol. 29, no. 6, pp. 33–41, 1984.
- [13] P. Pati, G. Jaume, L. A. Fernandes, A. Foncubierta-Rodríguez, F. Feroce, A. M. Anniciello, G. Scognamiglio, N. Brancati, D. Riccio, M. D. Bonito *et al.*, "Hact-net: A hierarchical cell-to-tissue graph neural network for histopathological image classification," in *Uncertainty for Safe Utilization of Machine Learning in Medical Imaging, and Graphs in Biomedical Image Analysis*. Springer, 2020, pp. 208–219.
- [14] B. Li, Y. Li, and K. W. Elliceiri, "Dual-stream multiple instance learning network for whole slide image classification with self-supervised contrastive learning," in *Proceedings of the IEEE/CVF Conference on Computer Vision and Pattern Recognition*, 2021, pp. 14 318–14 328.
- [15] W. Hou, L. Yu, C. Lin, H. Huang, R. Yu, J. Qin, and L. Wang, "H2-mil: Exploring hierarchical representation with heterogeneous multiple instance learning for whole slide image analysis," in *36th AAAI Conference on Artificial Intelligence*. AAAI Press, 2022.
- [16] T.-Y. Lin, P. Dollár, R. Girshick, K. He, B. Hariharan, and S. Belongie, "Feature pyramid networks for object detection," in *Proceedings of the IEEE conference on computer vision and pattern recognition*, 2017, pp. 2117–2125.
- [17] M. Tan, R. Pang, and Q. V. Le, "Efficientdet: Scalable and efficient object detection," in *Proceedings of the IEEE/CVF conference on computer vision and pattern recognition*, 2020, pp. 10 781–10 790.
- [18] D. Zhang, H. Zhang, J. Tang, M. Wang, X. Hua, and Q. Sun, "Feature pyramid transformer," in *European Conference on Computer Vision*. Springer, 2020, pp. 323–339.
- [19] W. Wang, E. Xie, X. Li, D.-P. Fan, K. Song, D. Liang, T. Lu, P. Luo, and L. Shao, "Pyramid vision transformer: A versatile backbone for dense prediction without convolutions," in *Proceedings of the IEEE/CVF International Conference on Computer Vision*, 2021, pp. 568–578.
- [20] H. Li, F. Yang, Y. Zhao, X. Xing, J. Zhang, M. Gao, J. Huang, L. Wang, and J. Yao, "Dt-mil: Deformable transformer for multi-instance learning on histopathological image," in *International Conference on Medical Image Computing and Computer-Assisted Intervention*. Springer, 2021, pp. 206–216.
- [21] Z. Shao, H. Bian, Y. Chen, Y. Wang, J. Zhang, X. Ji *et al.*, "Transmil: Transformer based correlated multiple instance learning for whole slide image classification," in *Advances in Neural Information Processing Systems*, vol. 34, 2021.
- [22] H. Zhang, Y. Meng, Y. Zhao, Y. Qiao, X. Yang, S. E. Coupland, and Y. Zheng, "Dtf-d-mil: Double-tier feature distillation multiple instance learning for histopathology whole slide image classification," in *Proceedings of the IEEE Conference on Computer Vision and Pattern Recognition*, 2022.
- [23] K. Simonyan and A. Zisserman, "Very deep convolutional networks for large-scale image recognition," *arXiv preprint arXiv:1409.1556*, 2014.
- [24] K. He, X. Zhang, S. Ren, and J. Sun, "Deep residual learning for image recognition," in *Proceedings of the IEEE conference on computer vision and pattern recognition*, 2016, pp. 770–778.
- [25] M. D. Zeiler and R. Fergus, "Visualizing and understanding convolutional networks," in *European conference on computer vision*. Springer, 2014, pp. 818–833.
- [26] T. G. Dietterich, R. H. Lathrop, and T. Lozano-Pérez, "Solving the multiple instance problem with axis-parallel rectangles," *Artificial intelligence*, vol. 89, no. 1-2, pp. 31–71, 1997.
- [27] M.-A. Carbonneau, V. Cheplygina, E. Granger, and G. Gagnon, "Multiple instance learning: A survey of problem characteristics and applications," *Pattern Recognition*, vol. 77, pp. 329–353, 2018.
- [28] X. Wang, Y. Yan, P. Tang, X. Bai, and W. Liu, "Revisiting multiple instance neural networks," *Pattern Recognition*, vol. 74, pp. 15–24, 2018.
- [29] A. Vaswani, N. Shazeer, N. Parmar, J. Uszkoreit, L. Jones, A. N. Gomez, Ł. Kaiser, and I. Polosukhin, "Attention is all you need," *Advances in neural information processing systems*, vol. 30, 2017.
- [30] M. Ilse, J. Tomczak, and M. Welling, "Attention-based deep multiple instance learning," in *International conference on machine learning*. PMLR, 2018, pp. 2127–2136.
- [31] A. Dosovitskiy, L. Beyer, A. Kolesnikov, D. Weissenborn, X. Zhai, T. Unterthiner, M. Dehghani, M. Minderer, G. Heigold, S. Gelly *et al.*, "An image is worth 16x16 words: Transformers for image recognition at scale," in *International Conference on Learning Representations*, 2020.
- [32] B. Zhou, A. Khosla, A. Lapedriz, A. Oliva, and A. Torralba, "Learning deep features for discriminative localization," in *Proceedings of the IEEE conference on computer vision and pattern recognition*, 2016, pp. 2921–2929.
- [33] D. Moitra and R. K. Mandal, "Classification of non-small cell lung cancer using one-dimensional convolutional neural network," *Expert Systems with Applications*, vol. 159, p. 113564, 2020.
- [34] E. H. Houssein, M. M. Emam, A. A. Ali, and P. N. Suganthan, "Deep and machine learning techniques for medical imaging-based breast cancer: A comprehensive review," *Expert Systems with Applications*, vol. 167, p. 114161, 2021.
- [35] P. Pati, G. Jaume, A. Foncubierta-Rodríguez, F. Feroce, A. M. Anniciello, G. Scognamiglio, N. Brancati, M. Fiche, E. Dubruc, D. Riccio *et al.*, "Hierarchical graph representations in digital pathology," *Medical image analysis*, vol. 75, p. 102264, 2022.
- [36] S. Ding, Z. Gao, J. Wang, M. Lu, and J. Shi, "Fractal graph convolutional network with mlp-mixer based multi-path feature fusion for classification of histopathological images," *Expert Systems with Applications*, p. 118793, 2022.
- [37] W. Shao, Z. Han, J. Cheng, L. Cheng, T. Wang, L. Sun, Z. Lu, J. Zhang, D. Zhang, and K. Huang, "Integrative analysis of pathological images and multi-dimensional genomic data for early-stage cancer prognosis," *IEEE transactions on medical imaging*, vol. 39, no. 1, pp. 99–110, 2019.
- [38] O.-J. Skrede, S. De Raedt, A. Kleppe, T. S. Hveem, K. Liestøl, J. Maddison, H. A. Askautrud, M. Pradhan, J. A. Nesheim, F. Albrechtsen *et al.*, "Deep learning for prediction of colorectal cancer outcome: a discovery and validation study," *The Lancet*, vol. 395, no. 10221, pp. 350–360, 2020.
- [39] R. M. Bremnes, T. Dønnem, S. Al-Saad, K. Al-Shibli, S. Andersen, R. Sirera, C. Camps, I. Martinez, and L.-T. Busund, "The role of tumor stroma in cancer progression and prognosis: Emphasis on carcinoma-associated fibroblasts and non-small cell lung cancer," *Journal of Thoracic Oncology*, vol. 6, no. 1, pp. 209–217, 2011.
- [40] K.-H. Yu, C. Zhang, G. J. Berry, R. B. Altman, C. Ré, D. L. Rubin, and M. Snyder, "Predicting non-small cell lung cancer prognosis by fully automated microscopic pathology image features," *Nature communications*, vol. 7, no. 1, pp. 1–10, 2016.
- [41] B. Fu, P. Liu, J. Lin, L. Deng, K. Hu, and H. Zheng, "Predicting invasive disease-free survival for early stage breast cancer patients using follow-up clinical data," *IEEE Transactions on Biomedical Engineering*, vol. 66, no. 7, pp. 2053–2064, 2019.
- [42] A. A. Alizadeh, V. Aranda, A. Bardelli, C. Blanpain, C. Bock, C. Borowski, C. Caldas, A. Califano, M. Doherty, M. Elsner *et al.*, "Toward understanding and exploiting tumor heterogeneity," *Nature medicine*, vol. 21, no. 8, pp. 846–853, 2015.
- [43] M. Y. Lu, D. F. Williamson, T. Y. Chen, R. J. Chen, M. Barbieri, and F. Mahmood, "Data-efficient and weakly supervised computational

- pathology on whole-slide images,” *Nature biomedical engineering*, vol. 5, no. 6, pp. 555–570, 2021.
- [44] J. Deng, W. Dong, R. Socher, L.-J. Li, K. Li, and L. Fei-Fei, “Imagenet: A large-scale hierarchical image database,” in *2009 IEEE conference on computer vision and pattern recognition*. IEEE, 2009, pp. 248–255.
 - [45] J. L. Ba, J. R. Kiros, and G. E. Hinton, “Layer normalization,” *arXiv preprint arXiv:1607.06450*, 2016.
 - [46] S. G. Zadeh and M. Schmid, “Bias in cross-entropy-based training of deep survival networks,” *IEEE Transactions on Pattern Analysis and Machine Intelligence*, vol. 43, no. 9, pp. 3126–3137, 2021.
 - [47] D. R. Cox, “Partial likelihood,” *Biometrika*, vol. 62, no. 2, pp. 269–276, 1975.
 - [48] P. Liu, B. Fu, S. X. Yang, L. Deng, X. Zhong, and H. Zheng, “Optimizing survival analysis of xgboost for ties to predict disease progression of breast cancer,” *IEEE Transactions on Biomedical Engineering*, vol. 68, no. 1, pp. 148–160, 2021.
 - [49] N. L. S. T. R. Team, “The national lung screening trial: overview and study design,” *Radiology*, vol. 258, no. 1, pp. 243–53, 2011.
 - [50] C. Kandoth, M. D. McLellan, F. Vandin, K. Ye, B. Niu, C. Lu, M. Xie, Q. Zhang, J. F. McMichael, M. A. Wyczalkowski, M. D. M. Leiserson, C. A. Miller, J. S. Welch, M. J. Walter, M. C. Wendl, T. J. Ley, R. K. Wilson, B. J. Raphael, and L. Ding, “Mutational landscape and significance across 12 major cancer types,” *Nature*, vol. 502, pp. 333 – 339, 2013.
 - [51] M. Zaheer, S. Kottur, S. Ravanbakhsh, B. Poczos, R. R. Salakhutdinov, and A. J. Smola, “Deep sets,” *Advances in neural information processing systems*, vol. 30, 2017.
 - [52] P. J. Heagerty and Y. Zheng, “Survival model predictive accuracy and roc curves,” *Biometrics*, vol. 61, no. 1, pp. 92–105, 2005.